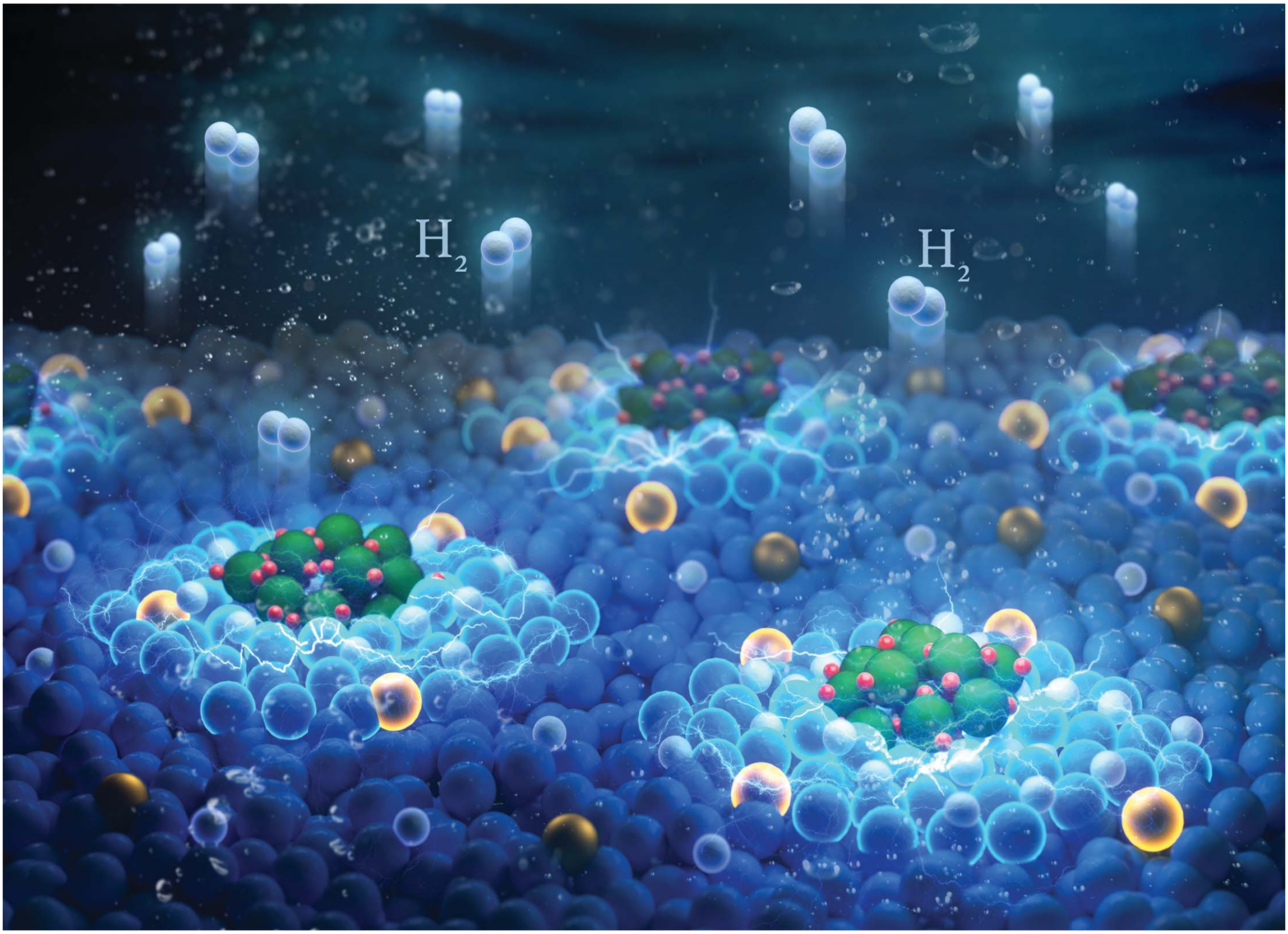

Showcasing research from Dr. Sung Ki Cho's laboratory, Center of Hydrogen and Fuel Cells, Korea Institute of Science and Technology, Seoul, Republic of Korea.

A MoO_x-incorporated RuAu composite electrocatalyst for the hydrogen evolution reaction in proton exchange membrane water electrolysis

Electrocatalytic activity of RuAu for hydrogen evolution reaction (HER) is improved by incorporating MoOx into the electrocatalyst. RuAu-MoO_x composite prepared through facile electrodeposition outperforms Ru and RuAu. Theoretical analyses demonstrate MoO_x finely modulated the H-binding free energy of nearby Ru, which realizes the lowest overpotential. Proton exchange membrane water electrolysis cell with RuAu-MoO_x exhibited a high performance with a superior mass activity of electrocatalyst.

Image reproduced by permission of Jong Hyun Jang, Hyun S. Park and Sung Ki Cho, *J. Mater. Chem. A*, 2025, **13**, 19316.

As featured in:

See Jong Hyun Jang,
Hyun S. Park, Sung Ki Cho *et al.*,
J. Mater. Chem. A, 2025, **13**, 19316.

ROYAL SOCIETY
OF **CHEMISTRY**

rsc.li/materials-a

Journal of
Materials Chemistry A

ROYAL SOCIETY
OF CHEMISTRY

PAPER

View Article Online
View Journal | View Issue

Check for updates

Cite this: *J. Mater. Chem. A*, 2025, **13**, 19316

A MoO_x-incorporated RuAu composite electrocatalyst for the hydrogen evolution reaction in proton exchange membrane water electrolysis†

Jaewon Lee,[ab] Jinho Oh,[ab] Junhyeong Kim,[a] Hee-Young Park,[a] Sung Jong Yoo,[a] Hyung-Kyu Lim,[c] Jong Hyun Jang,*[abd] Hyun S. Park*[ab] and Sung Ki Cho*[a]

In the water electrolysis system, Pt is commonly utilized as an electrocatalyst material for the hydrogen evolution reaction (HER). However, the scarcity and high cost of Pt pose challenges for the industrialization of PEMWE. This study proposes a MoO_x-incorporated RuAu composite as an efficient HER electrocatalyst for proton-exchange-membrane water electrolysis (PEMWE). The RuAu alloy electrocatalyst, containing less than 10% molybdenum oxide (RuAu-MoO_x) with an atomically uniform distribution, was successfully synthesized *via* co-electrodeposition. X-ray diffraction and X-ray photoelectron spectroscopy analyses revealed that the RuAu-MoO_x catalyst was composed of nanometer-sized crystallites and that high-valence states of Mo species interacted with the Ru and Au atoms, influencing their electronic structure. The electrocatalytic properties of RuAu-MoO_x were evaluated under acidic conditions, by varying the amount of MoO_x incorporated in the deposits. By fine-tuning the atomic composition of RuAu-MoO_x, an *iR*-compensated overpotential of 34.1 mV at −10 mA cm^{-2} for the HER was achieved with high stability of the electrocatalyst, outperforming Ru and RuAu. In addition, density functional theory calculations revealed that the synergistic effect of Au substitution and MoO_x incorporation optimized the electronic structure of the surface metal atoms for the HER, including hydrogen adsorption. When RuAu-MoO_x was applied to PEMWE as a catalyst for the cathode, it exhibited high performance (4.55 A cm^{-2} at 2 V) and superior mass activity (7.56 A mg^{-1} at 1.8 V) compared to the other Ru-related catalysts. This study highlights RuAu-MoO_x as an effective HER catalyst and suggests that it is a promising substitute for Pt in PEMWE.

Received 14th February 2025
Accepted 1st May 2025

DOI: 10.1039/d5ta01235j

rsc.li/materials-a

1. Introduction

The massive use of fossil fuels as energy sources is considered the most prominent cause of global warming.[1,2] As a fulfillment of the commitment to a net-zero emission, the generation of electricity from renewable energy sources has been steadily increasing. In 2020, global renewable energy production had reached 7600 TW h, representing an approximately 85% increase compared to the production in 2010. In the context of renewable energy utilization, hydrogen is receiving significant attention as a carbon-free energy carrier, owing to its high energy density (120 MJ kg^{-1}) and minimal environmental impact.[3–6] Water electrolysis is a promising energy conversion method for producing high-purity hydrogen by only consuming electrical energy and water.[7] Low-temperature water electrolysis can be classified into three types: alkaline water electrolysis, proton exchange membrane water electrolysis (PEMWE), and anion exchange membrane water electrolysis. Compared to other technologies, PEMWE offers advantages such as high current density operation, dynamic response capability, and the production of high-purity hydrogen with high efficiency, making it one of the most promising water electrolysis technologies.[8]

As a half reaction of water-splitting, the hydrogen evolution reaction (HER) should have a low overpotential for an efficient PEMWE. According to the Sabatier principle, an electrocatalyst with moderate hydrogen adsorption energy, neither too strong nor too weak, is considered a promising candidate for the HER.[9] In this regard, HER electrocatalysts that exhibit high catalytic activity with appropriate hydrogen adsorption energy are adapted in PEMWE.[10] Platinum (Pt) is considered to have the best characteristics for the HER due to its proper hydrogen adsorption energy.[11–14] However, its high cost and scarcity

---

[a] *Center for Hydrogen and Fuel Cells, Korea Institute of Science and Technology (KIST), Seoul 02792, Republic of Korea. E-mail: jhjang@kist.re.kr; hspark@kist.re.kr; skcho@kist.re.kr*

[b] *Division of Energy & Environment Technology, KIST School, University of Science and Technology (UST), Seoul, 02792, Republic of Korea*

[c] *Division of Chemical Engineering and Bioengineering, Kangwon National University, Chuncheon 24341, Republic of Korea*

[d] *Graduate School of Energy and Environment, KU-KIST Green School, Korea University, Seoul 02841, Republic of Korea*

† Electronic supplementary information (ESI) available. See DOI: **https://doi.org/10.1039/d5ta01235j**

hinder its use in green hydrogen production by PEMWE.[15,16] Ruthenium (Ru), a member of the Pt group metals, is noted for its similar hydrogen adsorption energy compared to that of Pt, implying high HER activity while being less expensive than Pt.[9] These characteristics make Ru a promising alternative to Pt. However, the catalytic activity of Ru is still lower than that of Pt, and numerous studies have been conducted to enhance its HER activity.

Alloying is one of the most common strategies for improving the activity of Ru, and various Ru alloys such as RuCo, RuNi, RuAu, and so on, have been developed.[17–19] Combining Ru with other heteroelements modifies the electronic structure of the electrocatalysts, which enables more favorable hydrogen adsorption and desorption on the Ru surface by tuning the hydrogen adsorption energy closer to that of Pt compared to pure Ru catalysts. Among various Ru alloys, RuAu has gained great attention due to the effective modification of the hydrogen adsorption energy as well as its enhanced stability against the HER, originating from the chemically inert characteristics of Au.[19–22] Despite its enhanced HER activity, the hydrogen adsorption characteristics of RuAu is still not optimum as the hydrogen adsorption energy shifts from −0.42 eV (Ru) to −0.38 eV (RuAu) while that of Pt is −0.17 eV, which increases the need for further modulation of the hydrogen adsorption energy.

In addition to alloying, the 3d electronic structure of Ru can be modified by interacting with metal oxides through the introduction of oxygen vacancies in the structure or chemical bonds between Ru and O.[23] Recently, molybdenum oxide (MoO_x) has been reported to enhance catalytic performance of Ru through the composite formation.[24,25] In this study, we sought to optimize the hydrogen adsorption energy of the Ru-based electrocatalyst by the simultaneous formation of its alloy and composite, thereby inducing fine-tuning of the electronic structure.

Among various techniques for the synthesis of Ru electrocatalysts, such as hydro/solvothermal synthesis, annealing, and physical/chemical vapor deposition, electrodeposition is a facile method for the introduction of foreign elements into the electrocatalyst *via* co-deposition.[26–29] Electrodeposition can produce desired metal alloys and metal composites by varying electrochemical conditions, such as electrolyte composition, potential, substrate, and electrochemical technique.[30–34] In this study, we synthesized a RuAu alloy decorated with MoO_x (RuAu-MoO_x) *via* electrodeposition and evaluated its HER activity and durability in acidic media. The changes in the HER activity of RuAu-MoO_x were investigated through various electrochemical analyses. Additionally, the electrocatalysts were applied to the cathode in a PEMWE cell to evaluate their catalytic activity and durability within the water electrolysis system and to explore their potential application in a PEMWE system.

2. Experimental

2.1 Preparation of the electrocatalysts

The electrolyte for RuAu-MoO_x electrodeposition was composed of 250 mM perchloric acid ($HClO_4$, 70%, Sigma-Aldrich) aqueous solution containing 20 mM ruthenium(III) chloride hydrate ($RuCl_3 \cdot xH_2O$, 99.98%, Sigma-Aldrich), 1 mM gold(III) chloride trihydrate ($HAuCl_4 \cdot 3H_2O$, ≥ 99.9%, Sigma-Aldrich), and various concentration of sodium molybdate (Na_2MoO_4, anhydrous, 99.9%, Sigma-Aldrich) as precursors for Ru, Au, and Mo, respectively. The detailed compositions of the solution are listed in Table S1†, including the nomenclature of the deposited electrocatalyst. A homemade Ti rotating disk electrode (RDE, 3 mm diameter), Ti foil (250 μm thickness, 99.7%, Sigma-Aldrich), and Ti felt (250 μm thickness, 60% porosity, 20 μm fiber diameter, 2PTL9N-025, Bekaert) were used as substrates for electrodeposition. A Pt wire and Ag/AgCl (saturated KCl) electrode were used as a counter and reference electrode, respectively. The reference electrode was rinsed with DI water before and after use and was immersed in the electrolyte only during the measurement to prevent cross-contamination of the electrolyte and saturated KCl solution. As a pretreatment, the Ti RDE was polished using alumina powder (Al_2O_3, particle size 0.3 μm) or a micro-cloth pad. To remove native oxide on the surface of the substrate, Ti foil and Ti felt were immersed in 5 wt% oxalic acid (99.5–100.2%, Daejung) aqueous solution at 70 °C for 30 min, and then rinsed with DI water and dried in air. The electrocatalysts were electrodeposited by applying a potential of −0.353 V (*vs.* RHE) for 100 s *via* using a HCP-803 potentiostat (Biologic). After electrodeposition, the electrode was rinsed with DI water. For the comparison, Pt/C catalyst was loaded on a GC RDE (5 mm dia.) following a reported procedure, and the loading amount of Pt was 100 μg cm^{-2}.[35]

2.2 Characterization of the electrocatalysts

The surface morphologies and the elemental compositions of the electrocatalysts were analyzed using field-emission scanning electron microscopy (FE-SEM, Hitachi, Regulus8230) and energy-dispersive X-ray spectroscopy (EDS; Oxford, Ultim Max). Transmission electron microscopy (TEM, Titan 80-300™, Thermo Fisher Scientific) was used to identify crystal structures and morphologies of the electrocatalysts. Energy-dispersive X-ray spectroscopy (EDS, Elite T Super, GATAN) was used to analyze the elemental distribution in the electrocatalyst. The chemical states of Ru, Au, and Mo in the electrocatalyst were analyzed through X-ray photoelectron spectroscopy (XPS, Nexsa, Thermo Fisher Scientific, monochromatic 1486.6 eV Al Kα X-ray source). Prior to the analysis, the surface of electrocatalysts was cleaned using Ar^+ (2 kV, 1 × 1 mm^2, 20 s sputtering). The sample chamber was maintained under ultimate vacuum ($<2 \times 10^{-8}$ Pa). Survey scans were acquired with a 400 μm spot size over a wide range of binding energies of 1–1400 eV. High-resolution (0.1 eV) scans of Ru, Au, and Mo were obtained with each narrow scan range. Thin-film X-ray diffraction (XRD) measurements (D Max 2500, Rigaku) were conducted to investigate the crystal structures and phases of RuAu-MoO_x composites, using a Cu Kα radiation source with a wavelength of 1.5406 Å, operating at 40 kV and 200 mA.

2.3 Electrochemical measurements

The activity of the electrocatalysts toward the HER was evaluated using a three-electrode electrochemical cell as described below. An electrocatalyst-deposited Ti RDE was used as a working electrode. An Ag/AgCl electrode and graphite rods were used as reference and counter electrodes, respectively. 1 M H_2SO_4 (95.0–98.0%, Sigma-Aldrich) aqueous solution was used as an electrolyte for the electrocatalytic activity measurements. Before all measurements, the electrolyte was purged with N_2 flow for 30 min, and the flow was maintained during the experiment. All electrochemical measurements were conducted using an HCP-803 potentiostat (Biologic). The potentials were calibrated with respect to the reversible hydrogen electrode (RHE). Polarization curves were obtained by linear sweep voltammetry (LSV) in 1 M H_2SO_4 in the potential range from open circuit potential to −0.15 V (*vs.* RHE) at a scan rate of 5 mV s^{-1}. Obtained curves were corrected with ohmic resistance, which is measured through electrochemical impedance spectroscopy (−0.05 V *vs.* RHE, 10^5–10^{-1} Hz, an amplitude of 18 mV). The stability was tested through chronopotentiometry at a cathodic current density of −10 mA cm^{-2} for 48 h. During all the measurements, the Ti RDE was connected to a modulated speed rotator (MSR rotator, Pine research) and rotated at 1600 rpm. The electrochemical active surface area was measured by CV in the potential range from 0.15–0.25 V (*vs.* RHE) at the scan rates of 5, 10, 25, 50, and 100 mV s^{-1} to obtain the double layer capacitance and relative surface area of each electrocatalyst. There was no rotation of the working electrode during the electrochemically active surface area (ECSA) measurements.

The activities of the electrocatalysts were also evaluated in a PEMWE cell. The membrane electrode assembly (MEA) consisted of electrocatalyst-deposited Ti felt as the cathode and Pt@IrO_2-electrodeposited Ti felt as the anode, prepared as explained in the cited literature, and a Nafion membrane (NR-212, Dupont™).[36] The MEA was fabricated by sandwiching a membrane between two electrodes, followed by hot pressing (120 °C, 395 psi, for 2 min), and its geometric area was 1 cm^2. The prepared MEA was placed between two current-collector plates with a serpentine flow channel. During the water electrolysis operation, the temperature of the PEMWE unit-cell and DI water (18.2 MΩ, injected into the anode at a flow rate of 15 ml min^{-1}) was maintained at 80 °C. Electrochemical measurements were performed using a potentiostat (HCP-803, Biologic). Before all measurements, the MEA was activated by applying 1.55 V for 30 min. The polarization curves were obtained by LSV from open circuit voltage to 2.2 V at a scan rate of 10 mV s^{-1}. As a stability test, chronopotentiometry at a current density of 1 A cm^2 was conducted for 48 h. The EIS measurements were conducted in a frequency range of 10^5–10^{-1} Hz at an amplitude of 18 mV.

2.4 Computational methods

Density functional theory (DFT) calculations were performed using the Vienna *Ab initio* Simulation Package.[37] The interaction between the electrons and ions was described using the projector augmented wave pseudopotential method with a plane-wave cutoff energy of 400 eV.[38] The generalized gradient approximation-type Perdew–Burke–Ernzerhof functional was employed to account for the exchange-correlation energy.[39] A Monkhorst–Pack *k*-point mesh was used for Brillouin zone sampling, with the specific grid density adjusted according to the system size.[40] Geometry optimizations were performed until the atomic forces were less than 0.01 eV $Å^{-1}$ and the total energy convergence was below 10^{-5} eV. All the calculations were spin-polarized, and dipole corrections were applied to account for the asymmetry of the slab models. A constant value (0.24 eV) was added to the H-binding energy derived from the electronic energy to account for the zero-point energy and entropy changes.[41]

3. Results and discussion

3.1 Characterization of the Ru, RuAu, and RuAu-MoO_x electrodeposits

To characterize the electrodeposition of RuAu-MoO_x, CVs of the electrolytes containing either individual elemental precursors or a mixture of all precursors were measured (Fig. S1†). In the case of individual precursors, the current peaks for the reduction of the precursors were observed at 0.047 V (*vs.* RHE) for Ru, 0.797 V for Au, and −0.153 V for Mo, respectively (Fig. S1a†), and similar responses were also observed elsewhere.[42–44] When all the elemental precursors were present, multiple peaks attributed to the reduction of individual elements were observed in the CV (Fig. S1b†). Furthermore, the large reduction current began to flow at approximately −0.003 V, indicating that the elements electrodeposited during the negative potential sweep served as the electrocatalyst for the HER. The applying potential was set to −0.353 V (*vs.* RHE) to ensure the reduction of all precursors. During electrodeposition, noisy current responses were observed (Fig. S1c†), which were attributed to the formation and subsequent detachment of hydrogen bubbles on the electrocatalyst surface.

The amount of Mo content in the RuAu-MoO_x electrocatalyst was controlled by changing the concentration of the Mo precursor in the electrolyte from 1 to 5 mM. The electrodeposited RuAu-MoO_x electrocatalysts are denoted according to the concentration of the Mo (Table S1†). Fig. 1 shows the SEM images of the surface morphologies of Ru, RuAu, and RuAu-MoO_x with various amounts of the Mo precursor. All the catalysts were composed of small granules with diameters in the range of several hundred nanometers. Upon the addition of the Mo precursors to the electrolyte, uniformly distributed small nanoparticles of approximately a few nanometers in size were observed on the catalyst surface. This suggests that the addition of the Mo precursors might increase the surface area of the electrocatalyst. EDS analyses revealed that the Mo content remained below 10 at% relative to Ru, and the atomic ratio of Mo to Ru gradually increased with Mo precursor concentration (Fig. 1h and Table S2†).

Fig. 2 shows the TEM image of the RuAu-2MoO_x composite. EDS elemental mapping analyses confirmed that Ru, Au, and Mo were uniformly distributed across all areas. Consistent with the SEM-EDS results, Ru, which exhibited the highest content, showed the strongest EDS signal, whereas Mo exhibited a relatively low signal intensity. The interplanar spacing observed in the TEM image corresponded primarily to the Ru (101) plane,

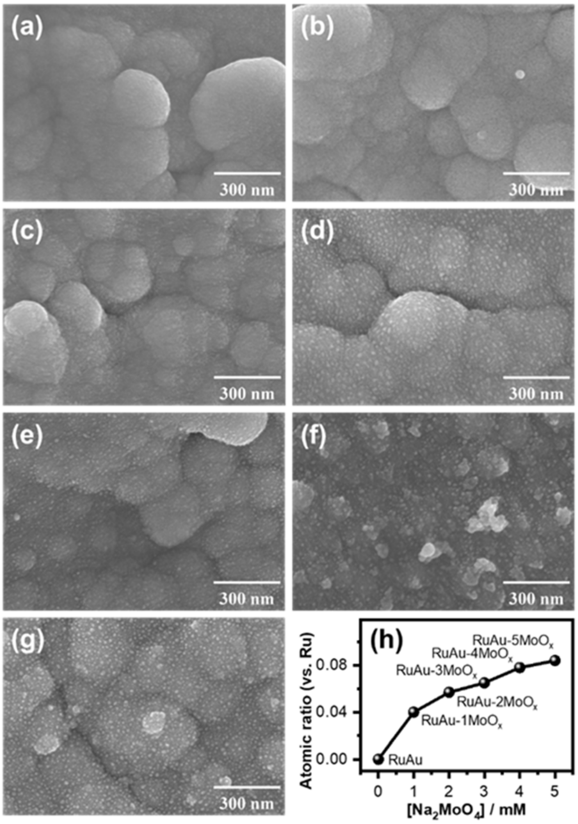

Fig. 1 Top view SEM images of (a) Ru, (b) RuAu, and (c–g) RuAu-1–5MoO$_x$ deposits on Ti foil. (h) Plot of the atomic ratio of Mo to Ru.

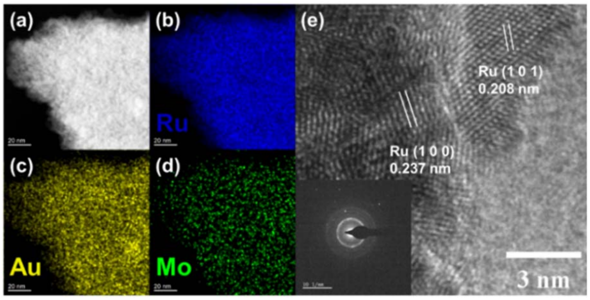

Fig. 2 TEM images of the RuAu-2MoO$_x$ deposit: (a–d) images of elemental mapping and (e) corresponding images of the RuAu-2MoO$_x$ deposit. The insets show a selected-area electron diffraction pattern of (e).

with a spacing of approximately 0.208 nm, although the Ru (100) plane was also detected. Most observed crystalline phases were identified as Ru crystals. The selected area electron diffraction pattern revealed ring patterns corresponding to the Ru (100) or Ru (101) planes (hexagonal close-packed Ru metal, ICDD PDF# 04-003-6760). No lattice or ring patterns attributable to the crystalline phases of Au or MoO$_x$ were observed. Based on the TEM analysis, Ru exists in a nanocrystalline state within the composite, whereas Au and MoO$_x$ are either incorporated into the Ru lattice or exist in an amorphous state.

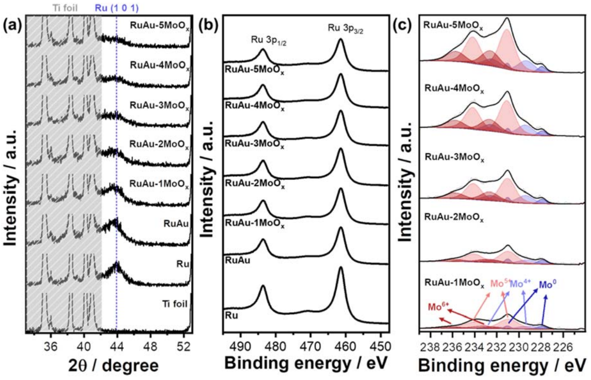

Fig. 3 (a) X-ray diffraction patterns of Ru, RuAu, and RuAu-1–5MoO$_x$ deposits on Ti foil. (b) Ru 3p XPS spectra and (c) Mo 3d XPS spectra of RuAu-1–5MoO$_x$ deposits on Ti foil.

Fig. 3a presents the XRD patterns of Ru, RuAu, and RuAu-MoO$_x$ electrodeposited on Ti foil. Most of the diffraction peaks were identified as crystalline phases of the Ti substrate (Fig. S2†). In the pattern of the Ru deposit, a peak at 43.8° was observed, corresponding to the (101) plane of the hcp-structured Ru metal (ICDD PDF# 04-003-6760). For RuAu and RuAu-MoO$_x$, a decrease in intensity, broadening, and a slight negative shift were observed for this peak. The decrease in intensity and broadening of the peak suggest a decrease in the crystal size, while the negative peak shift indicates an increase in the interplanar spacing. Calculations based on Bragg's law and the Scherrer equation revealed that the addition of both Au and MoO$_x$ increased the interplanar spacing of the (101) plane of Ru and decreased its crystal size (Table S3†). No distinct XRD peaks corresponding to Au or MoO$_x$ were observed, suggesting that these elements did not form separate crystalline phases, which is consistent with the TEM analysis results.

XPS was performed to investigate the chemical states of each element. In the Ru 3p spectrum, a peak corresponding to Ru 3p$_{3/2}$ was observed at 461.33 eV, along with a satellite peak at 470.9 eV (Fig. S3†), and a peak of Ru 3d$_{5/2}$ appeared at 280.0 eV (Fig. S4†), which confirms that Ru exists in a metallic state in all the electrodeposits.[45] For Au, the signal for Au 4f$_{7/2}$ was observed near 84.1 eV, which indicates that Au also exists in a metallic state across all electrodeposits (Fig. S5†).[46,47] It should be noted that the peak shifts of Ru and Au, previously reported for RuAu alloys, were not observed in this study.[19,21] This discrepancy might originate from differences in the synthesis methods, as previous studies used laser ablation or calcination, rather than electrodeposition, as employed in this study.[19,42] Instead, the weak shift of the Ru 3d peak in a positive direction (by 0.04 eV for RuAu-5MoO$_x$ with respect to RuAu) was observed as the Mo content increased (Fig. S4†). This peak shift suggests that MoO$_x$ affects the electronic structure of adjacent Ru.

The change in the Mo peak is more significant, as shown in Fig. 3b. The analyses of the Mo 3d peaks of the deposits solely from the Mo precursors revealed that Mo has valence states of Mo^{4+} or Mo^{5+} (Fig. S6†), indicating that the Mo precursor was not reduced to metallic Mo at the electrodeposition potential (−0.353 V *vs.* RHE) and was transformed to the oxide deposit, which is consistent with other studies.[48] It is noted that the standard reduction potential for MoO_4^{2-} to metallic Mo is −0.913 V (*vs.* RHE).[48,49] As the Mo precursor concentration increased, the intensity of the Mo signal in the XPS spectra gradually increased, which would further affect the electronic structure of RuAu. The Mo spectra of the composites indicate that Mo exists in various oxidation states, including Mo^0, Mo^{4+}, Mo^{5+}, and Mo^{6+}.[50,51] Furthermore, based on the area ratio of each peak in the Mo 3d spectra, it was confirmed that MoO_x species predominantly existed in high-valence states (Mo^{5+} and Mo^{6+}, Fig. S7†), which was found consistently even after HER operation (Fig. S8†). Meanwhile, the presence of Mo^{5+} suggests the formation of MoO_{3-x} with oxygen vacancies, indicating that RuAu-MoO_x contains abundant oxygen vacancies for all Mo precursor concentrations, as confirmed by the O 1s spectra of RuAu-MoO_x (Fig. S9†).[52] It is also consistent with the recent study, which reported that electrodeposited MoO_x contained plenty of oxygen vacancies in the deposit.[49] Mo^{5+} and oxygen vacancies are known to facilitate charge transfer, thus improving the HER performance of Ru-MoO_x.[53,54]

3.2 Analysis of the electrocatalytic activity with respect to the HER

The changes in the activity and stability of the RuAu-MoO_x electrocatalysts according to the MoO_x content were evaluated electrochemically (Fig. 4). The *iR*-corrected LSV curves revealed that the addition of MoO_x enhanced HER activity, which was maximized for RuAu-2MoO_x (Fig. 4a). The HER overpotential (η) for RuAu-2MoO_x was 34.1 mV, which was lower by 7.1 mV at −10 mA cm^{-2} and by 9.4 mV at −50 mA cm^{-2} than that for RuAu (inset of Fig. 4a), although it was still higher than that for Pt/C (20 mV for 0.1 mg_{Pt} cm^{-2}). In the stability test, by applying a constant current of −10 mA cm^{-2} for 48 hours, the negligible potential increase within the range from 6.3 to 18 mV for all electrocatalysts while RuAu-2MoO_x showed the smallest increase (6.3 mV), which might be due to gradual leaching of Mo species (Fig. S10†), indicating that RuAu-2MoO_x electrocatalysts are relatively stable among others (Fig. 4b). The Tafel slopes of the RuAu-MoO_x electrocatalysts with various Mo contents were obtained from the *j*–*V* curves (Fig. 4c). Compared to Tafel slopes of Ru (43.9 mV dec^{-1}) and RuAu (40.8 mV dec^{-1}), RuAu-MoO_x exhibited a lower Tafel slope (38.7–40.2 mV dec^{-1}, listed in Table S4†). The Tafel slope of RuAu-MoO_x implies that HER on RuAu-MoO_x electrocatalysts follows the Volmer–Heyrovsky route while the HER on Pt/C catalyst is based on the Volmer–Tafel mechanism with a Tafel slope of 24.8 mV dec^{-1}, which is consistent with previously reported values.[55] Fig. 4d presents the Nyquist plots for the RuAu-MoO_x electrocatalyst, which show a clear difference in the charge transfer resistance, whereas the ohmic resistance is nearly identical across all electrocatalysts. Fitting with the Randles equivalent circuit model provided the corresponding values (Table S5†), where RuAu–2MoO_x exhibited the lowest charge-transfer resistance, which is consistent with the LSV results.

SEM analyses showed the formation of surface protrusions in the electrocatalysts with the addition of Mo (Fig. 1). The ECSA was analyzed to investigate the change in the area-normalized electrocatalytic activity of RuAu-MoO_x, through CV measurement on the charging current in the non-faradaic region (Fig. S11†). As expected, the charging current slightly increases with the addition of MoO_x to the electrocatalyst. From the linear relationship between the charging current and scan rate, the linearly fitted slope of the plot of the charging current density against the scan rate is proportional to the double-layer capacitance (Fig. S12†). The double-layer capacitance gradually

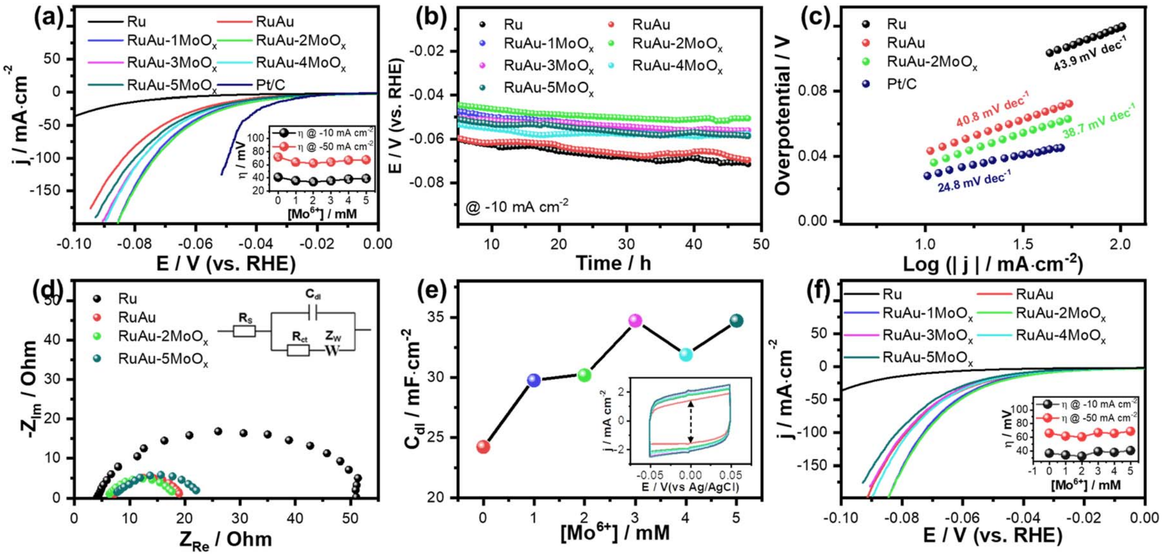

Fig. 4 (a) *iR*-compensated LSV curves. (b) Chronopotentiometry response at a current density of −10 mA cm^{-2} during 48 hours of operation. (c) Tafel plots. (d) EIS measurement at an overpotential of −50 mV (*vs.* RHE). The inset shows the Randles equivalent circuit model. (e) The plot of double-layer capacitance (C_{dl}) measured from cyclic voltammetry (inset) along with the concentration of the Mo precursor. (f) Surface area normalized LSV. For RuAu-2MoO_x, the amounts of Ru, Au, and Mo in the electrocatalyst (electrodeposited for 100 s) were approximately 43, 8, and 2.7 μg cm^{-2}, respectively.

increases with increasing MoO_x content (Fig. 4e and S13). The relative surface area of RuAu-MoO_x with respect to the surface area of Ru was calculated (Table S6†), and accordingly, surface area-normalized LSV results were obtained (Fig. 4f). Even after the area-normalization, an enhancement in activity was still observed with the addition of MoO_x, and RuAu-2MoO_x exhibited the lowest overpotential (inset of Fig. 4f). These results demonstrate that the incorporation of MoO_x into RuAu enhances HER performance by modifying the intrinsic electrocatalytic activity.

3.3 DFT calculation

To gain a deeper insight into the enhanced HER activity of the RuAu-MoO_x catalysts, we conducted comprehensive DFT calculations. The computational model is based on a Ru (001) surface with Au substitutions ($RuAu_1$, $RuAu_2$, and $RuAu_3$) and adsorbed MoO_x clusters derived from the MoO_3 bulk structure (Fig. 5a). We systematically varied the oxidation state of Mo from Mo^{6+} to Mo^0 to investigate its impact on catalyst activity, mirroring the experimentally observed variations in the Mo oxidation states. The H-binding free energy (ΔG_H) was calculated for various active sites on these catalyst models, focusing on Au-substituted regions and Ru regions distant from Au substitutions (Fig. 5b–d). In bare catalysts without MoO_x clusters, increasing the Au content generally weakened H-binding on the Ru sites, which is consistent with previous studies on RuAu alloys.[19] Notably, the Ru–Au boundary regions emerged as the most favorable active sites, where Au moderately weakened the H-binding. However, in the $RuAu_3$ model, the 3-fold site between the Au atoms showed significantly weakened H-binding, indicating a return to the intrinsic H-binding properties of Au.

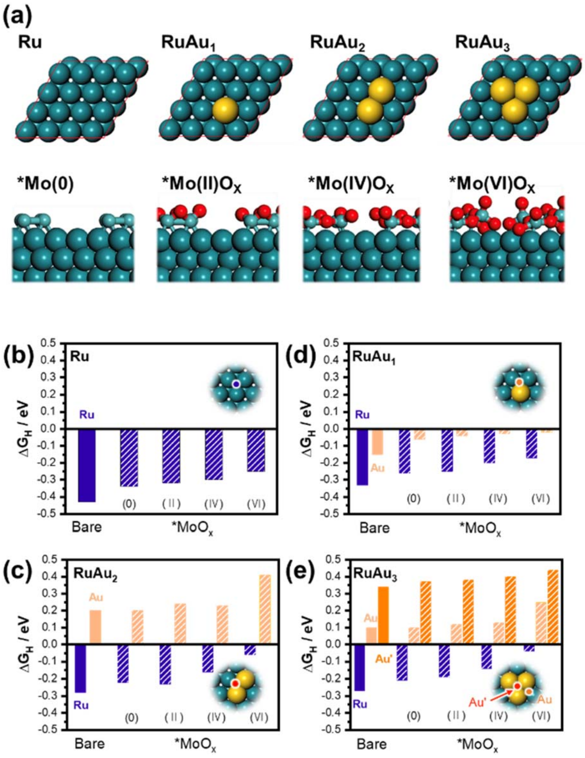

Fig. 5 (a) Atomic structures of RuAu surfaces with varying Au content and adsorbed MoO_x clusters with different oxidation states. H-binding free energies (ΔG_H) for various active sites on (b) Ru, (c) $RuAu_1$, (d) $RuAu_2$, and (e) $RuAu_3$ surfaces with and without MoO_x clusters. Blue bars represent Ru sites, orange bars represent Au sites, and hatched bars indicate sites affected by MoO_x.

The introduction of MoO_x clusters decreased ΔG_H across all active sites, aligning well with our experimental observations. The calculation also reveals a clear trend: higher Mo oxidation states led to decreased ΔG_H across all active sites. Note that the main Mo oxidation states in RuAu-MoO_x were relatively high. This trend can be attributed to the electronic modification of the surface metal atoms by MoO_x. Interestingly, our calculations showed a transition in the most active HER sites with increasing Au content. In the $RuAu_1$ model, the sites adjacent to Au exhibited the highest HER activity. However, from $RuAu_2$ onwards, the H-binding on the Au sites becomes too weak, causing the Ru regions to emerge as the primary active sites for the HER. This suggests a synergistic effect between Au and MoO_x that boosts the HER activity of the dominant Ru surface regions. This is also supported by the experimental observation that the increase in MoO_x amount and subsequent increase in its surface coverage (Fig. S14†) over a certain level (equivalent to the level at 2 mM of the Mo precursor) decreases the HER activity. This synergistic effect can be explained by a combination of two factors: (1) Au atoms weaken the initially strong H-binding on Ru, bringing it closer to the optimal value for the HER and (2) MoO_x clusters further tune the electronic structure of Ru atoms, optimizing their H-binding energy. This delicate balance results in a catalyst in which the majority of the surface (Ru regions) becomes highly active for the HER, rather than just the Au–Ru interface or Au sites. Such a design principle could lead to a more efficient use of the catalyst surface area and potentially higher overall catalytic activity.

To elucidate the electronic origin of these trends, the d-band centers of surface metal atoms were analyzed. A strong linear correlation between the d-band center values and ΔG_H is observed for all cases (Fig. S15†), consistent with the d-band theory.[56] The presence of MoO_x induces a downshift in the d-band center, with higher Mo oxidation states causing a more pronounced downshift. This can be attributed to the formation of stable bonding states between the metal d-band and the oxygen 2p orbital at lower energy levels as the oxygen content increases (Fig. S16†). This d-band center downshift has significant implications for catalytic activity. As the d-band center moves away from the Fermi level, the antibonding states of the metal-adsorbate interaction become more occupied, leading to a weaker binding of hydrogen. In the case of Ru, which typically binds hydrogen too strongly for optimal HER activity, this weakening of the binding brings ΔG_H closer to the ideal value of 0 eV. The varying oxidation states of Mo in MoO_x further fine-tune this effect, allowing for precise control of the electronic structure, and consequently, the catalytic activity. This synergistic effect between the MoO_x clusters and RuAu surface resulted in a catalyst with optimized electronic properties for the HER, explaining the enhanced activity observed in our experiments.

3.4 Overall water splitting

RuAu-2MoO$_x$, which exhibited superior catalytic activity than Ru and RuAu for the HER in half-cell experiments, was used as an electrocatalyst for the cathode in a single cell for PEMWE. Fig. 6a shows a schematic diagram of the PEMWE cell using the RuAu-2MoO$_x$ electrocatalyst. RuAu-2MoO$_x$, Ru, and RuAu deposits were formed on the Ti felt surface by applying the same potential (−0.353 V *vs.* RHE) used in the half-cell evaluation. Fig. 6b shows the performance of the overall water splitting reaction when Ru, RuAu, and RuAu-2MoO$_x$ were used as catalysts for the cathode. At a cell voltage of 2 V, the current densities were 4.54 A cm^{-2} for RuAu-2MoO$_x$, 4.08 A cm^{-2} for RuAu, and 3.53 A cm^{-2} for Ru, respectively, demonstrating that RuAu-2MoO$_x$ has the highest HER catalytic activity in the PEMWE cell as well as in the three-electrode cell. PEIS analysis at 1.5 V was performed to investigate the HER overpotential for Ru, RuAu, and RuAu-2MoO$_x$. The ohmic resistance of the unit cell is approximately 55 mΩ, with no significant differences observed among the three catalysts. The semicircles in each Nyquist plot are attributed to the charge-transfer resistance at the interfaces between the cathode, anode, and membrane. The lower-frequency region on the right side of the plot shows a high resistance for the oxygen evolution reaction, while the high-frequency region corresponds to the HER-related resistances. The HER resistances are 0.325 Ω for Ru, 0.168 Ω for RuAu, and 0.031 Ω for RuAu-2MoO$_x$, indicating that RuAu-2MoO$_x$ effectively reduces HER-related charge-transfer resistance and consequently decreases the overall charge transfer resistance for the water splitting reaction. Fig. 6d presents the stability of the catalyst materials under PEMWE operating conditions, as shown by a 48-h chronoamperometric evaluation at 1 A cm^{-2}.

As illustrated, the catalysts formed on the Ti PTL *via* electrodeposition exhibited excellent durability, with no increase in overpotential, even after prolonged exposure to the reaction conditions.

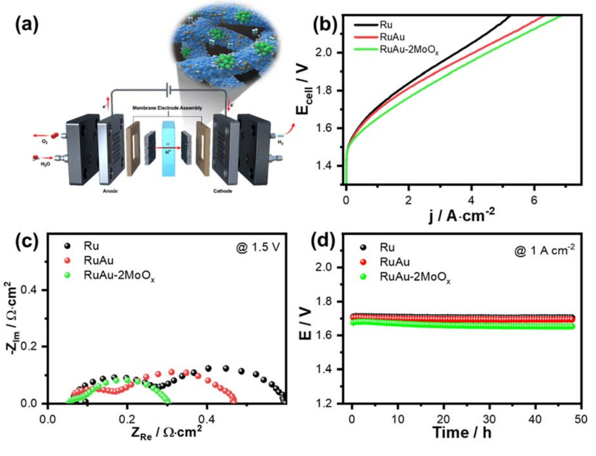

Fig. 6 Electrochemical measurements for Ru, RuAu, and RuAu-2MoO$_x$ as the electrocatalyst for the HER in PEMWE. (a) Schematic diagram of the PEMWE unit cell with the RuAu-MoO$_x$ electrocatalyst. (b) j-V curves of the PEMWE cell. (c) Nyquist plots with an amplitude of 18 mV and an applied voltage of 1.5 V. (d) Chronopotentiometry response at a current density of 1 A cm^{-2} during 48 hours of operation.

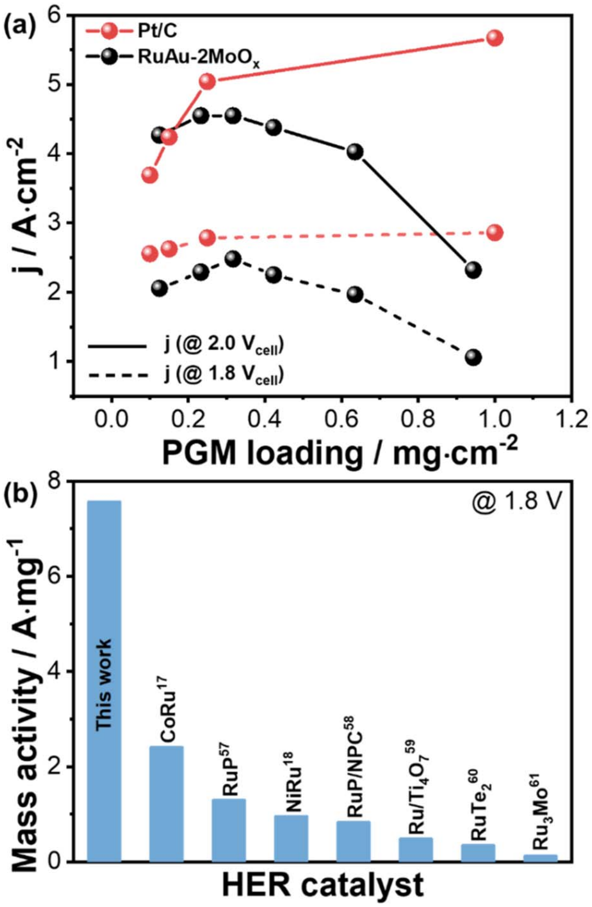

Fig. 7 (a) The performance of PEMWE cells loaded with RuAu-2MoO$_x$ or Pt/C at the cell voltages of 1.8 and 2.0 V with various catalyst loading amounts. (b) The comparison of the performance at 1.8 V with values reported in the literature dealing with Ru-related HER electrocatalysts.

Fig. 7a shows the comparison of the performance of PEMWE cells loaded with RuAu-2MoO$_x$ and Pt/C at various loading amounts. The performance of the cell loaded with the RuAu-2MoO$_x$ catalyst, while not superior to that of the cell loaded with a Pt catalyst, demonstrates comparable efficiency and, under certain measurement conditions, even surpasses the performance of the Pt-based cell. Unlike Pt, the performance of the RuAu-2MoO$_x$ catalyst-based cell exhibited a gradual decrease with increasing catalyst loading. This decline is likely attributed to the increased cell resistance associated with the thicker RuAu-2MoO$_x$ catalyst layer. Fig. 7b shows the comparison of the performance of PEMWE cells loaded with RuAu-2MoO$_x$ and Ru-related HER catalysts in the literature.[17,18,57–61] Detailed information on the cell condition (operating temperature, membrane, and anode catalyst) is presented in Table S7.† RuAu-2MoO$_x$ exhibited the highest mass activity compared to that of reported Ru-related HER catalysts. These results indicate that RuAu-MoO$_x$ is a promising HER electrocatalyst.

4. Conclusions

This study investigated the HER characteristics of RuAu-MoO$_x$ composites. Through co-electrodeposition, a RuAu-MoO$_x$

electrocatalyst was formed with a uniform distribution of all the elements across the surface. The elemental ratios of the catalysts varied depending on the concentration of the Mo precursor, and the approximate composition was Ru : Au : Mo = 1 : 0.2 : 0.06. Ru and Au were in the metallic form, whereas, owing to its more negative reduction potential compared to the other precursors, Mo primarily existed as Mo^{5+} in the form of MoO_x within the catalyst layer. The catalyst was evaluated for HER activity in a 1 M H_2SO_4 solution, demonstrating an *iR*-compensated overpotential of 34.1 mV at −10 mA cm^{-2}, which was 7.1 mV lower than that of RuAu, confirming the enhancement in activity. The RuAu-MoO_x composite exhibited a Tafel slope of 38.7 mV dec^{-1}, which is the lowest among all Ru and RuAu catalysts, indicating superior HER kinetics. ECSA measurements confirmed that the increase in catalytic activity was not mainly attributed to the increased surface area but rather to a change in the intrinsic activity of the catalyst. DFT analysis demonstrated that the increase in the intrinsic activity originated from the downshift of the *d*-band center with the incorporation of MoO_x onto RuAu, which induced an optimal shift in the H-binding free energy. The RuAu-MoO_x catalyst applied in the PEMWE cell exhibited superior overall water electrolysis performance compared to Ru and RuAu catalysts, achieving remarkable cell performance and higher mass activity than those for cells with Ru-related HER catalysts. The RuAu-2MoO_x composite, with its excellent activity and reduced noble metal content, shows great potential as an HER catalyst for PEMWE applications.

Data availability

All relevant data are available in this article and the ESI.†

Author contributions

Jaewon Lee: investigation, writing – original draft. Jinho Oh: validation. Junhyeong Kim: data curation. Hee-Young Park: visualization. Sung Jong Yoo: resources. Hyung-Kyu Lim: formal analysis. Jong Hyun Jang: funding acquisition, project administration. Hyun S. Park: conceptualization, writing – review and editing. Sung Ki Cho: methodology, supervision, writing – review and editing.

Conflicts of interest

There are no conflicts to declare.

Acknowledgements

This research was supported by the National R&D Program through the National Research Foundation of Korea (NRF) funded by the Ministry of Science and ICT (RS-2024-00409901 and RS-2024-00431630). This study was supported by the Korea Institute of Science and Technology (grant numbers 2K02970 and 2E33281).

Notes and references

1 S. Chu and A. Majumdar, *Nature*, 2012, **488**, 294–303.
2 L. Al-Ghussain, *Environ. Prog. Sustainable Energy*, 2019, **38**, 13–21.
3 B. Johnston, M. C. Mayo and A. Khare, *Technovation*, 2005, **25**, 569–585.
4 C. Tarhan and M. A. Çil, *J. Energy Storage*, 2021, **40**, 102676.
5 M. R. Usman, *Renew. Sustain. Energy Rev.*, 2022, **167**, 112743.
6 T.-Z. Ang, M. Salem, M. Kamarol, H. S. Das, M. A. Nazari and N. Prabaharan, *Energy Strat. Rev.*, 2022, **43**, 100939.
7 S. S. Kumar and H. Lim, *Energy Rep.*, 2022, **8**, 13793–13813.
8 W. Li, H. Tian, L. Ma, Y. Wang, X. Liu and X. Gao, *Mater. Adv.*, 2022, **3**, 5598–5644.
9 Y. Yang, Y. Yu, J. Li, Q. Chen, Y. Du, P. Rao, R. Li, C. Jia, Z. Kang and P. Deng, *Nanomicro Lett.*, 2021, **13**, 1–20.
10 M. Carmo, D. L. Fritz, J. Mergel and D. Stolten, *Int. J. Hydrogen Energy*, 2013, **38**, 4901–4934.
11 K. J. Choi and S.-K. Kim, *Int. J. Hydrogen Energy*, 2023, **48**, 849–863.
12 H. Kim, S. Choe, H. Park, J. H. Jang, S. H. Ahn and S.-K. Kim, *Nanoscale*, 2017, **9**, 19045–19049.
13 G. Shi, H. Yano, D. A. Tryk, S. Nohara and H. Uchida, *Phys. Chem. Chem. Phys.*, 2019, **21**, 2861–2865.
14 M. Zhou, Y. Zhao, X. Zhao, P.-F. Yin, C.-K. Dong, H. Liu, X.-W. Du and J. Yang, *ACS Appl. Energy Mater.*, 2024, **7**, 3848–3857.
15 S. Zhang, X. He, Y. Ding, Z. Shi and B. Wu, *Renew. Sustain. Energy Rev.*, 2024, **204**, 114821.
16 K. Ojha, S. Saha, P. Dagar and A. K. Ganguli, *Phys. Chem. Chem. Phys.*, 2018, **20**, 6777–6799.
17 T. Lee, Y. Park, H. Kim, Y. K. Hong, E. Hwang, M. Kim, S. K. Kim and D. H. Ha, *Int. J. Energy Res.*, 2022, **46**, 7975–7987.
18 K.-R. Yeo, H. Kim, K.-S. Lee, S. Kim, J. Lee, H. Park and S.-K. Kim, *Appl. Catal., B*, 2024, **346**, 123738.
19 T. Kwon, A. Yu, S.-j. Kim, M. H. Kim, C. Lee and Y. Lee, *Appl. Surf. Sci.*, 2021, **563**, 150293.
20 Q. Lu, A.-L. Wang, Y. Gong, W. Hao, H. Cheng, J. Chen, B. Li, N. Yang, W. Niu and J. Wang, *Nat. Chem.*, 2018, **10**, 456–461.
21 C. H. Chen, D. Wu, Z. Li, R. Zhang, C. G. Kuai, X. R. Zhao, C. K. Dong, S. Z. Qiao, H. Liu and X. W. Du, *Adv. Energy Mater.*, 2019, **9**, 1803913.
22 V. Giulimondi, S. K. Kaiser, A. J. Martín, S. Büchele, F. Krumeich, A. H. Clark and J. Pérez-Ramírez, *Small*, 2022, **18**, 2200224.
23 B. Zhang, X. Zheng, O. Voznyy, R. Comin, M. Bajdich, M. García-Melchor, L. Han, J. Xu, M. Liu and L. Zheng, *Science*, 2016, **352**, 333–337.
24 H. Zeng, S. Chen, Y. Q. Jin, J. Li, J. Song, Z. Le, G. Liang, H. Zhang, F. Xie and J. Chen, *ACS Energy Lett.*, 2020, **5**, 1908–1915.
25 P. Jiang, Y. Yang, R. Shi, G. Xia, J. Chen, J. Su and Q. Chen, *J. Mater. Chem. A*, 2017, **5**, 5475–5485.
26 K. Shah, R. Dai, M. Mateen, Z. Hassan, Z. Zhuang, C. Liu, M. Israr, W. C. Cheong, B. Hu and R. Tu, *Angew. Chem.*, 2022, **134**, e202114951.

27 T. Luo, J. Huang, Y. Hu, C. Yuan, J. Chen, L. Cao, K. Kajiyoshi, Y. Liu, Y. Zhao and Z. Li, *Adv. Funct. Mater.*, 2023, **33**, 2213058.
28 Y. Li, L. A. Zhang, Y. Qin, F. Chu, Y. Kong, Y. Tao, Y. Li, Y. Bu, D. Ding and M. Liu, *ACS Catal.*, 2018, **8**, 5714–5720.
29 D. D. Megersa, G. T. Gudena, Y. Kim and H. K. Yu, *Adv. Sustain. Syst.*, 2023, **7**, 2300257.
30 T. Boiadjieva-Scherzer, H. Kronberger, G. Fafilek and M. Monev, *J. Electroanal. Chem.*, 2016, **783**, 68–75.
31 H. Li, Q. Tang, B. He and P. Yang, *J. Mater. Chem. A*, 2016, **4**, 6513–6520.
32 S. Shetty, M. M. J. Sadiq, D. K. Bhat and A. C. Hegde, *J. Electroanal. Chem.*, 2017, **796**, 57–65.
33 Y. Ullal and A. C. Hegde, *Int. J. Hydrogen Energy*, 2014, **39**, 10485–10492.
34 T. Byk, T. Gaevskaya and L. Tsybulskaya, *Surf. Coat. Technol.*, 2008, **202**, 5817–5823.
35 J. N. Hansen, H. Prats, K. K. Toudahl, N. Mørch Secher, K. Chan, J. Kibsgaard and I. Chorkendorff, *ACS Energy Lett.*, 2021, **6**, 1175–1180.
36 A. Lim, J. Kim, H. J. Lee, H.-J. Kim, S. J. Yoo, J. H. Jang, H. Y. Park, Y.-E. Sung and H. S. Park, *Appl. Catal., B*, 2020, **272**, 118955.
37 G. Kresse and J. Furthmüller, *Phys. Rev. B:Condens. Matter Mater. Phys.*, 1996, **54**, 11169.
38 P. E. Blöchl, *Phys. Rev. B:Condens. Matter Mater. Phys.*, 1994, **50**, 17953.
39 J. P. Perdew, K. Burke and M. Ernzerhof, *Phys. Rev. Lett.*, 1996, **77**, 3865.
40 H. J. Monkhorst and J. D. Pack, *Phys. Rev. B:Condens. Matter Mater. Phys.*, 1976, **13**, 5188.
41 J. K. Nørskov, T. Bligaard, A. Logadottir, J. Kitchin, J. G. Chen, S. Pandelov and U. Stimming, *J. Electrochem. Soc.*, 2005, **152**, J23.
42 R. Zou, Y. Wang, M. Hu, Y. Wei and T. Fujita, *J. Phys. Chem. C*, 2022, **126**, 4329–4337.
43 G. Gotti, K. Fajerwerg, D. Evrard and P. Gros, *Electrochim. Acta*, 2014, **128**, 412–419.
44 J. You, D. Wu and H. Liu, *Polyhedron*, 1986, **5**, 535–537.
45 D. J. Morgan, *Surf. Interface Anal.*, 2015, **47**, 1072–1079.
46 J. Wang, H. Zhu, D. Yu, J. Chen, J. Chen, M. Zhang, L. Wang and M. Du, *ACS Appl. Mater. Interfaces*, 2017, **9**, 19756–19765.
47 H. Wu, X. Huang, M. Gao, X. Liao and B. Shi, *Green Chem.*, 2011, **13**, 651–658.
48 R. Syed, S. Ghosh, P. Sastry, G. Sharma, R. Hubli and J. Chakravartty, *Surf. Coat. Technol.*, 2015, **261**, 15–20.
49 W. Zhang, H. Li, C. J. Firby, M. Al-Hussein and A. Y. Elezzabi, *ACS Appl. Mater. Interfaces*, 2019, **11**, 20378–20385.
50 J. Baltrusaitis, B. Mendoza-Sanchez, V. Fernandez, R. Veenstra, N. Dukstiene, A. Roberts and N. Fairley, *Appl. Surf. Sci.*, 2015, **326**, 151–161.
51 P. Spevack and N. McIntyre, *J. Phys. Chem.*, 1992, **96**, 9029–9035.
52 C. Li, H. Jang, M. G. Kim, L. Hou, X. Liu and J. Cho, *Appl. Catal., B*, 2022, **307**, 121204.
53 J. Cai, J. Ding, D. Wei, X. Xie, B. Li, S. Lu, J. Zhang, Y. Liu, Q. Cai and S. Zang, *Adv. Energy Mater.*, 2021, **11**, 2100141.
54 Z. Luo, R. Miao, T. D. Huan, I. M. Mosa, A. S. Poyraz, W. Zhong, J. E. Cloud, D. A. Kriz, S. Thanneeru and J. He, *Adv. Energy Mater.*, 2016, **6**, 1600528.
55 J. Wang, H. Y. Tan, T. R. Kuo, S. C. Lin, C. S. Hsu, Y. Zhu, Y. C. Chu, T. L. Chen, J. F. Lee and H. M. Chen, *Small*, 2021, **17**, 2005713.
56 B. Hammer and J. K. Nørskov, *Surf. Sci.*, 1995, **343**, 211–220.
57 D. Galyamin, J. Torrero, J. D. Elliott, I. Rodríguez-García, D. G. Sánchez, M. A. Salam, A. S. Gago, M. Mokhtar, J. L. Gómez de la Fuente and S. V. Bueno, *Adv. Energy Sustain. Res.*, 2023, **4**, 2300059.
58 R. Ma, Y. Wang, G. Li, L. Yang, S. Liu, Z. Jin, X. Zhao, J. Ge and W. Xing, *Nano Res.*, 2021, **14**, 4321–4327.
59 S. Zhao, S.-F. Hung, L. Deng, W.-J. Zeng, T. Xiao, S. Li, C.-H. Kuo, H.-Y. Chen, F. Hu and S. Peng, *Nat. Commun.*, 2024, **15**, 2728.
60 Z. Zhang, C. Jiang, P. Li, K. Yao, Z. Zhao, J. Fan, H. Li and H. Wang, *Small*, 2021, **17**, 2007333.
61 Z. Zhang, P. Li, Q. Wang, Q. Feng, Y. Tao, J. Xu, C. Jiang, X. Lu, J. Fan and M. Gu, *J. Mater. Chem. A*, 2019, **7**, 2780–2786.